Desalination and Water Treatment
www.deswater.com
doi: 10.5004/dwt.2023.29972

311 (2023) 1–9
November

Behavior of calcium carbonate growth during low-temperature multi-effect distillation seawater desalination

Dongdong Liu[a,b], Daquan Zhang[a,b,*], Tingting Zhang[a], Yijie Cai[a]

[a]*Shanghai Key Laboratory of Materials Protection and Advanced Materials in Electric Power, Shanghai University of Electric Power, Shanghai 201306, China, emails: zhangdaquan@shiep.edu.cn (D.Q. Zhang), naruseumi@163.com (D.D. Liu), 18800207301@163.com (T.T. Zhang), 1397827276@qq.com (Y.J. Cai)*
[b]*Shanghai Engineering Research Centre of Energy-Saving in Heat Exchange Systems, Shanghai 200090, China*

Received 26 April 2023; Accepted 11 September 2023

ABSTRACT

The low-temperature multi-effect distillation desalination (LT-MED) is an intriguing and advancing trend in the desalination process. However, calcium carbonate scale ($CaCO_3$) can have lasting adverse consequences in heat-exchange tube in the LT-MED desalination system. It destructively affect the heat transfer and the water production efficiency. $CaCO_3$ exhibit differences in the different environmental factors. Behaviour during operating pressure of LT-MED of calcium carbonate growth are unknown. This paper examines the influence of operation pressure on the precipitation of $CaCO_3$ scale. It demonstrates that the amount of scaling is reduced under pressure. The least amount of $CaCO_3$ scale is formed under the operation pressure of 60 kPa. The distribution probability of large particles of $CaCO_3$ is greater under operation pressure. The operation pressure does not change the $CaCO_3$ structure type. The structure of $CaCO_3$ is still calcite. The molecular dynamics simulation is used to study the formation process of $CaCO_3$ under different operation pressure. The formation mechanism about the $CaCO_3$ scale under different operation pressure in LT-MED is further discussed. These data provide a link between $CaCO_3$ behaviour during the experience of operation pressure.

Keywords: Seawater desalination; Operation pressure; Calcium carbonate ($CaCO_3$); Scale formation

1. Introduction

As the development of economy, the water demand for manufacturing, power generation and domestic sector is also increasing [1]. By 2050, the global water demand is projected to increase more than 55%. It will push 40% of the world population below water scarcity level. Seawater desalination can solve the shortage of fresh water and promote the sustainable development of economy and society. Many countries are already planning more seawater desalination projects up and down the coast [2]. Presently, there are more than 18.000 desalination plants in 150 countries which can produce roughly 38 billion·m^3 purified water per year. There are two main techniques including thermal evaporation/condensation and membrane filtration (SWRO) [3]. The operation and maintenance cost of SWRO is easily affected by the quality of feed water. Owing to the uncertainty of SWRO, thermal desalination methods are deemed as the dominant processes employed in desalination market [4]. Among the evaporation/condensation technique, the low-temperature multi-effect distillation (LT-MED) is one of the most efficient desalination methods [5]. The multi-effect distillation (MED) process consists of a series of stages (usually from 2 to 16) that are maintained at decreasing levels of pressure. Operating pressure is below normal atmospheric pressure. The temperature of the first stage

* Corresponding author.

is around 70°C, to be used to evaporate some of the brine inside the stage that is kept at low pressure. Fig. 1 shows a schematic diagram of the MED unit [6]. The key advantages of LT-MED desalination systems compared to other processes are low energy consumption and high productivity [7], due to low-temperature operation, the systems can utilize the waste heat from the thermal power plant and solar energy, which greatly reduce the embodied water consumption and increase economic benefits [8,9]. However, there are a lot of inorganic salts in seawater, such as Mg^{2+} and Ca^{2+} ions. They become crystallization fouling deposited on the surface of the heat exchange tube to form a dense scale layer. The scaling problem greatly affects the water production efficiency during the LT-MED process [10]. It seriously affects the heat transfer performance of the heat exchange tube, which greatly reduce the water production efficiency. Even, the scaling can also cause the under-deposit corrosion, resulting in perforation and leakage of the heat exchange tube. Thus, the influence of scaling seems to be crucial in LT-MED system and affects the quality of the product water.

There are many factors affecting the scaling, such as temperature, flow velocity, pH value and pressure [11]. The operation pressure can affect the formation of scales, such as calcium carbonate ($CaCO_3$), $CaSO_4$ and $BaSO_4$. As for $CaCO_3$ scaling, its deposition reaction is more obviously affected by pressure, owing to CO_2 participating in the chemical reaction. Dyer and Graham [12]. find that the oilfield scaling tendency of the carbonate and sulfate brines can decrease marginally with the increasing of the pressure (1,379–27,580 kPa). Ahmadi et al. [13]. further explored the reason that a pressure (101.325–6,282.15 kPa) drop can decrease the solubility of $CaCO_3$ and increase the saturation ratio for $CaCO_3$. However, the action mechanism of the operation pressure of the LT-MED process on the $CaCO_3$ scaling is still not clear and needs to be further investigated.

Herein, we explore the effect of the operation pressure of the LT-MED process on $CaCO_3$ scaling. The formation of $CaCO_3$ scale under different pressures (101.1, 80, 60 and 40 kPa) are tested by the static precipitation method and the electrochemical impedance spectroscopy test. The $CaCO_3$ scale is characterized by the Fourier-transform infrared spectroscopy (FTIR), and the scanning electron microscopy (SEM). The molecular dynamics simulations are used to analyze the $CaCO_3$ scale formation procedure. The growth model and the formation mechanism of $CaCO_3$ crystal under different operation pressure are discussed.

2. Materials and methods

2.1. Static precipitation method

The prepared solution containing Ca^{2+} and HCO_3^- was in accordance with the China National Standard (GB/T16632-2019). The prepared solution (6 mmol/L Ca^{2+} and 12 mmol/L HCO_3^-) were blended into a volumetric flask of 250 mL. The mild $Na_2B_4O_7$ buffer solution was added to keep the pH around 8. Then, the effects of different operation pressures on $CaCO_3$ deposition were investigated at a temperature of 60°C in a vacuum drying oven (10 h). The concentration of calcium ions was measured every 2 h. The sampling solution was filtered with medium speed quantitative filter paper. Then, 25 mL filtrate was moved into a conical flask (250 mL) and 80 mL water was added into the conical flask. The KOH solution (200 mg/L, 5 mL) and about 0.1 g of calcium-carboxylic acid indicator ($C_{21}H_{14}N_2O_7S$) was added into the mixed solution. It was titrated with ethylenediaminetetraacetic acid disodium salt solution ($C_{10}H_{14}N_2Na_2O_8$, EDTA-Na) until the color of solution changes from purple red to bright blue.

2.2. Electrochemical measurements

The working electrode was AA5052 Al alloy material (2.46 wt.% Mg, 0.27 wt.% Fe, 0.19 wt.% Cr, Cu 0.1 wt.% Cu, 0.1 wt.% Si, 0.06 wt.% Mn and balance Al) which exposed an area of 1 cm^2. Before the electrochemical measurement, the working electrode was polished with a series of SiC papers (600; 800; 1,000; 1,200; 1,500 and 2,000 grit), washed with deionized water and ethanol, and dried at room temperature. All the electrochemical measurements were tested on CHI660D electrochemical workstation. The scanning voltage range was from –0.5 to –1.8 V (vs. SCE) in linear sweep voltammetry and the scan rate was 2.0 mV/s [14]. After the open circuit potential was stable, the EIS measurement was performed and recorded at a frequency range of 10^5 to 10^{-2} Hz. The amplitude perturbation for EIS test was about 10 mV [13].

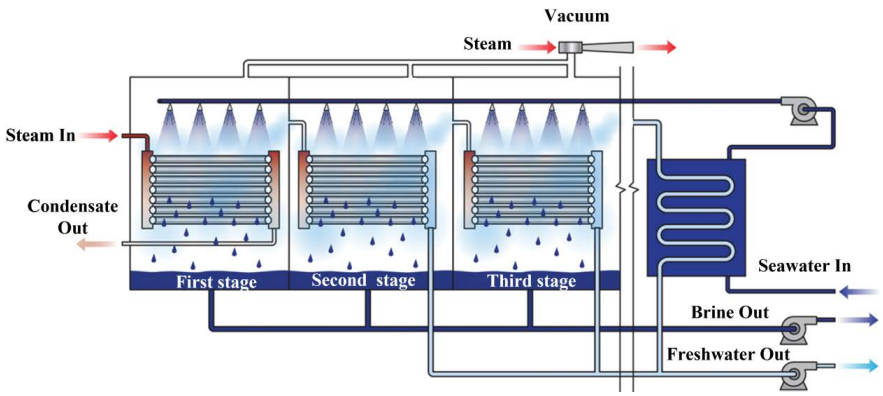

Fig. 1. Schematic of process of multi-effect distillation unit. Reprinted from the study of Al-Karaghouli and Kazmerski [6]. Copyright (2013), with permission from Elsevier.

2.3. Scale characterization

The $CaCO_3$ scale formed under the different pressure was further analyzed. Its precipitated phases were tested by X-ray diffraction (XRD) on an X-ray powder diffractometer (Bruker D8 Advance, Germany), and by infrared spectroscopy on an FTIR spectrophotometer (Nicolet iS20, Thermo Scientific, America). The crystal structure of $CaCO_3$ scale was studied by Raman spectroscopy (JYH R800, Horiba, France). The morphology of $CaCO_3$ was identified by SEM on a scanning electronic microscope (Sigma 300, Zeiss, Germany). The volume extent of $CaCO_3$ was measured by laser diffraction particle size analyzers (SALD-2201, Shimadzu, Japan).

2.4. Molecular dynamics simulation

The molecular dynamics simulations were built entirely within Materials Studio 2020. It consisted of water molecules, calcium ions and carbonate ions in a tetragonal unit cell. The system of simulations was programmed in the isothermal–isobaric ensemble (NPT), where P (ambient pressure) and T (temperature) are kept constant [15,16]. The temperature was 333 K. The pressures were 101.1, 80, 60 and 40 kPa, respectively. On the other hands, the CompassIIforce field was determined for modeling intermolecular atomic interactions. The time step was set at 1 fs, and the simulation ran for 50 ps [17].

3. Results and discussion

3.1. Static precipitation method

Three experiments are reported on for each set of pressure conditions. The calcium ion concentration in solution under different pressures are plotted in Fig. 2. The concentration of calcium ions (c_{Ca2+}) has the same trend of change under different pressures. The c_{Ca2+} in the solution decreases continuously with the increase of time. The reduced calcium ions in the solution are converted to the form of calcium carbonate. In other words, the more calcium ions left in the solution, the less calcium carbonate is produced. As shown in Fig. 2, the initial concentration of calcium ions is basically the same. The initial concentration of calcium ions is basically the same. The remaining concentration of calcium ions is the highest at 60 kPa, the scale formation of calcium carbonate is the smallest.

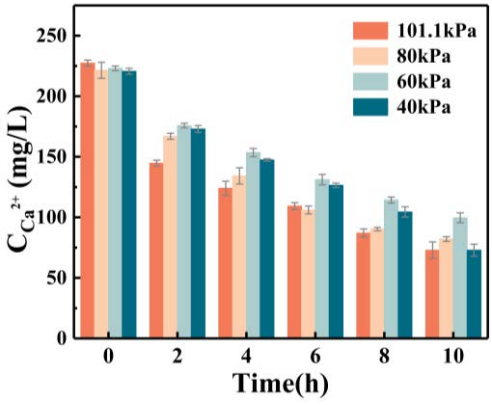

Fig. 2. Calcium ion concentration in solution under different pressures every 2 h.

3.2. Linear sweep voltammetry measurement

The linear sweep voltammetry curves are shown in Fig. 3a. The curves of Fig. 3a can be divided into two parts. The curves show a trend of rising steadily in the left part of inflection point. Then the curves rise steeply in the right part of inflection point. The left part of curves corresponds to a water reduction process. The right part of curves indicates a reaction dominated by an oxygen reduction process [18]. The reduction processes are as follows [19,20]:

$$O_2 + 2H_2O + 4e^- \rightarrow 4OH^- \quad (1)$$

$$2H_2O + 2e^- \rightarrow H_2 + 2OH^- \quad (2)$$

$$HCO_3^- + OH^- \rightarrow CO_3^{2-} + H_2O \quad (3)$$

$$CO_3^{2-} + Ca^{2+} \rightarrow CaCO_3(s) \quad (4)$$

From Eqs. (1) and (2), both the oxygen reduction process and the water reduction process can generate a large amount of OH^-. The pH near the cathodic electrode is increased. The generation of OH^- further react with HCO_3^- according to Eq. (3). It creates favorable conditions for CO_3^{2-} formation. With the concentration of CO_3^{2-} increasing, the electrode surface is deposited easily by $CaCO_3$ scale. It can be seen from Fig. 3a that the cathodic current under negative pressure is significantly higher than that under the 101.1 kPa at the same potential. The larger cathodic current density is obtained under 60 kPa. In previous research, the larger cathodic current density corresponds to less $CaCO_3$ scaling [21,22]. Therefore, the negative pressure is more favorable to decrease the formation of $CaCO_3$ scale. The deposition of $CaCO_3$ scale on the electrode surface is less under 60 kPa.

3.3. EIS measurements

The influence of pressure on electrochemical deposited $CaCO_3$ scale has been explored through EIS. Fig. 3b and c show the Nyquist and Bode plots under the different pressures. The depressed capacitive loops are observed for the electrode under the 101.1 kPa. As for electrode under negative pressure, a capacitive loop in the high frequency and a straight line (Warburg impedance) in the low frequency are observed. It is clear that the impedance response of the electrode has significantly changed under negative pressure. This indicates that the electrochemical reaction is being controlled by the mass transport rate. Usually, the deposited film formed on the surface of electrode is mainly composed of $CaCO_3$ scale layer and corrosion products [23]. The Warburg impedance is mainly because of the diffusion-controlled step of cations and other ions through the deposited film [24,25]. The impedance spectrum with only a depressed capacitive loop for Al electrode suggests a compact deposited film is formed can prevent the diffusion processes of ions. The impedance spectra are analyzed according to the equivalent circuits shown in Fig. 3d and e.

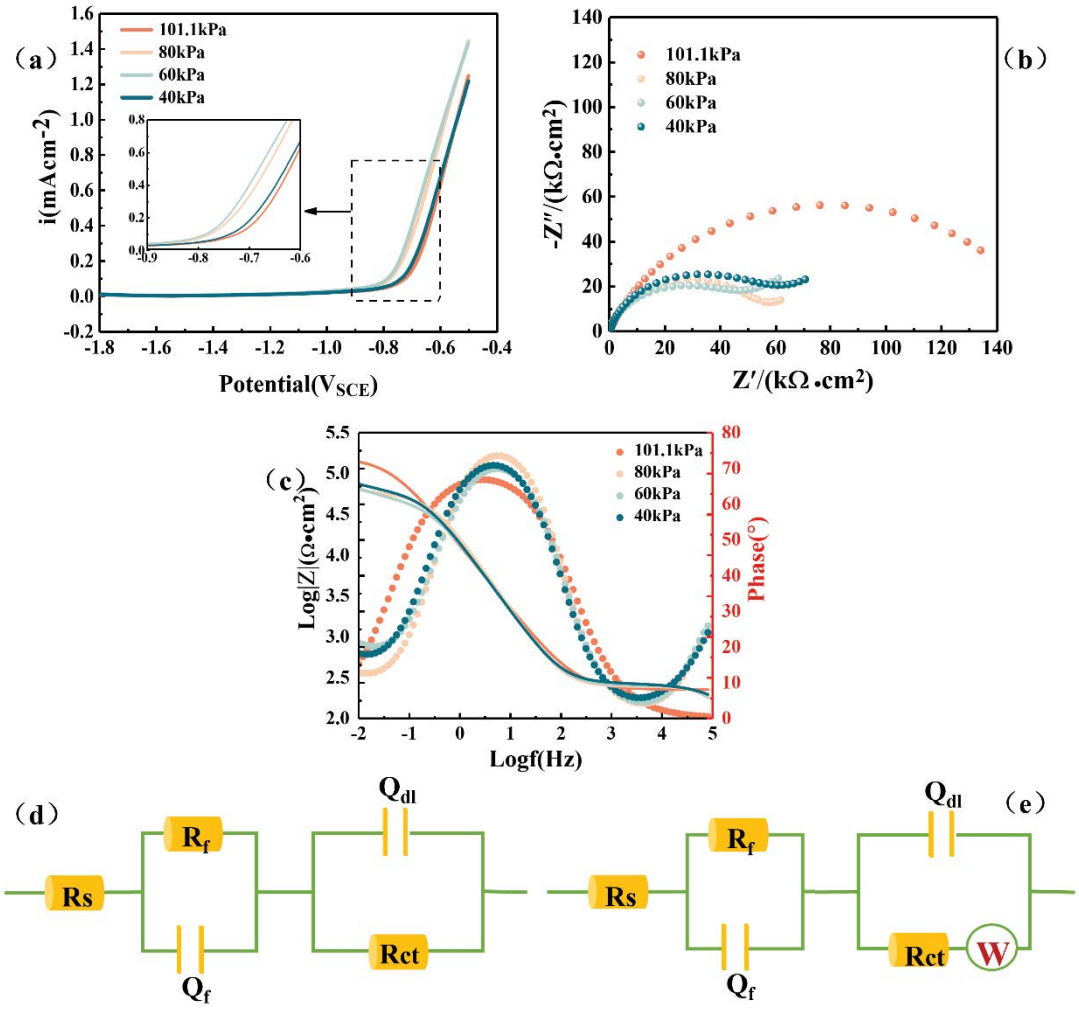

Fig. 3. LSV curves (a), Nyquist plots (b) and Bode plots (c) for aluminum electrode under different pressures (25°C); the equivalent circuit model for EIS at 101.1 kPa (d); the equivalent circuit model for EIS under negative pressure (e).

Table 1
Results of electrochemical parameters fitted in EIS for alloy in different pressures

Pressure (kPa)	R_s (kΩ/cm²)	Q_f		R_f (kΩ/cm²)	Q_{dl}		R_{ct} (kΩ/cm²)	R_p (kΩ/cm²)	W (μS/s$^{0.5}$·cm²)	χ^2 (10^{-4})
		Y_0 (μS/s^n·cm²)	n		Y_0 (μS/s^n·cm²)	n				
101.1	0.11	0.17	0.79	157.8	919.1	0.99	1.15	157.9	–	5.64
80	0.10	0.11	0.90	5.22	304.4	0.95	1.43	5.37	256.4	3.78
60	0.10	0.13	0.86	4.46	174.3	0.99	1.48	4.61	139.9	3.32
40	0.10	0.13	0.87	5.72	426.4	0.91	1.59	5.88	158.0	2.65

In the circuits, R_s represents the resistance of the solution, Q_{dl} is the constant phase element of the electrochemical double layer, and R_{ct} is the charge transfer resistance [26]. R_f are the resistance produced by the deposit film formed on the aluminum alloy surface and Q_f stands for its capacitive response. W is the Warburg impedance element. While R_p is the polarization resistance, which is approximately equal to the sum of R_{ct} and R_f. Table 1 shows the impedance parameters fitted by using the equivalent circuits under different pressures. The R_p under 101.1 kPa is the largest, indicating that the metal electrode is covered by the deposited film and the active area for electron transfer is restricted. With the decrease of the operation pressure, the value of R_p decreases significantly. This variation trend means that the nucleation and the growth of $CaCO_3$ scale slow down under the negative pressure. The lowest R_p value is obtained under 60 kPa, suggesting few $CaCO_3$ scale deposits on the electrode surface in this operation condition.

3.4. Scale characterization

The FTIR spectra are used to record the compositional information and structure of $CaCO_3$ scale [27]. Fig. S1 shows the typical FTIR spectra of the $CaCO_3$ scale obtained under different pressures. It is obvious that the FTIR spectra have no significant difference with the decrease of pressure. For the $CaCO_3$ scale obtained under negative pressure, the FTIR spectra have 874; 1,425; 712 and 1,792 cm^{-1} adsorption bands [28,29]. The characteristic absorption peak of 1,792 cm^{-1} is the vibration band of the C=O group. The peak at 874 cm^{-1} is strong and sharp. The peak of 712 cm^{-1} is sharp but not as strong as 874 cm^{-1}. They are all related to the C–O bending vibration. The peak at 874 cm^{-1} is out-plane bend of the CO_3^{2-} groups, and the peak at 712 cm^{-1} is in-plane bend of the CO_3^{2-} groups. The peak at 1,425 cm^{-1} is related to C–O asymmetric stretching vibration.

The XRD patterns of the $CaCO_3$ scale obtained under different pressures is shown in Fig. S2. Under normal pressure, there are some characteristic peaks of $CaCO_3$ scale and some miscellaneous peaks corresponding to other substances. These distinct characteristic peaks located at 2θ values of 22.8°, 29.17°, 36.08°, 39.11°, 42.96°, 47.23° and 48.5° correspond to calcite crystallographic planes (012), (104), (110), (113), (202), (018), and (116), respectively. And the miscellaneous peaks correspond to sodium chloride [30]. Under negative pressure, it also appears the same characteristic peak of $CaCO_3$. but there are no miscellaneous peaks. It indicates that the purity of calcium carbonate obtained under negative pressure is higher. In addition, the peak intensity located at 2θ values of 29.17° is obviously different. This is mainly due to the different crystallinity of calcium carbonate crystals under different pressures.

The crystal structure of $CaCO_3$ scale formed under different pressures is also studied by Raman spectroscopy, and the results are shown in Fig. S3. The Raman spectra of the $CaCO_3$ scale under different pressures have no apparent difference. The peaks at 153, 284 and 1,087 cm^{-1} are the characteristic bands of calcite [31]. This proves that the crystal form of the $CaCO_3$ scale is still calcite. The peak at 1,087 cm^{-1} is symmetric C–O stretching of the CO_3^{2-} groups. The peak at 153 and 284 cm^{-1} are corresponding to the lattice vibration of calcite.

The volume content distribution curves of the $CaCO_3$ scale formed under different pressures are shown in Fig. 4. The size of $CaCO_3$ scale has three optimum volumes content extremum under different pressures. The proportion of volume fraction between 0–2 μm under 101.1 kPa is higher than that under negative pressure. The volume fraction of $CaCO_3$ scale between 25–50 μm is the largest under 60 kPa. It shows that the average size of $CaCO_3$ scale under negative pressure is larger than that under normal pressure. The possible mechanism is reported as Oswald ripening [32,33]. That is, in the subsequent stage of the precipitation phase from the supersaturated solution, the particle size of the precipitation phase is not the same. With the smaller particles dissolving and the larger particles growing, the average particle size increases. The particle size of $CaCO_3$ scale formed after crystal nucleation is 0–2 μm and a part of $CaCO_3$ gathered particles due to Oswald ripening with the increase of reaction time so that the particles size of $CaCO_3$ scale increases to 35–40 μm. The average diameter of $CaCO_3$ particles formed under different pressures is shown Table 2. The $CaCO_3$ scale formed under 60 kPa has the biggest median diameter and the biggest mean diameter.

The SEM images of the $CaCO_3$ scale under different pressures are shown in Fig. 5. These morphologies have the subtle changes with the variation of the pressure. Under 101.1 kPa, the crystal of $CaCO_3$ scale is complete calcite structure. The shape of calcite is a complete rhombohedron. The rhombohedron particle has clear surface lines, complete crystal development, and regular particle surface. With the decrease of pressure, the shape of calcite becomes irregular rhombohedron. A small number of particles are seriously agglomerated, forming an amorphous large particle structure. The small particles are most likely to gather under 60 kPa and form particles with larger size.

3.5. Crystallization dynamics

Molecular simulation software is used to investigate the formation process of $CaCO_3$ crystals under the compass force field. The optimized results of solution under different pressures are shown in Fig. 6. The mean square displacement (MSD) of Ca^{2+} ions and the energy fluctuation curves are displayed in Fig. 7. The displacement change of particles with time can be expressed by the MSD ($A^{\circ 2}$), which reflects the diffusion of particles. The larger the MSD is, the faster particles move. For example, $r(t)$ represents the position of the particle at time t. And $r(0)$ represents the initial position of the particle. Then the MSD calculation formula is shown in Eq. (5). Where, "< >" represents the average value of all particles in the group. Furthermore, the detailed data of diffusion coefficient (D) of Ca^{2+} ions are obtained by Eq. (6) [34], which are shown in Table 3.

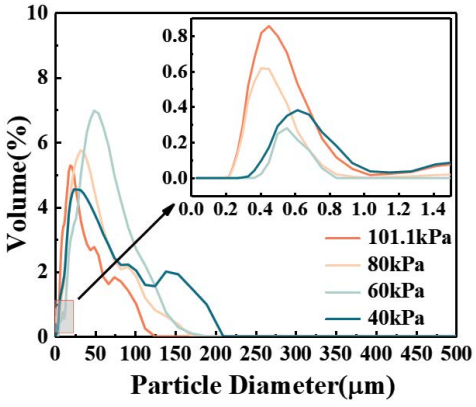

Fig. 4. Volume content curve.

Table 2
Average diameter of the calcium carbonate particle-size distribution

	101.1 kPa	80 kPa	60 kPa	40 kPa
Median D (μm)	17.65	27.91	41.47	28.34
Mean V (μm)	14.89	23.46	36.83	26.43

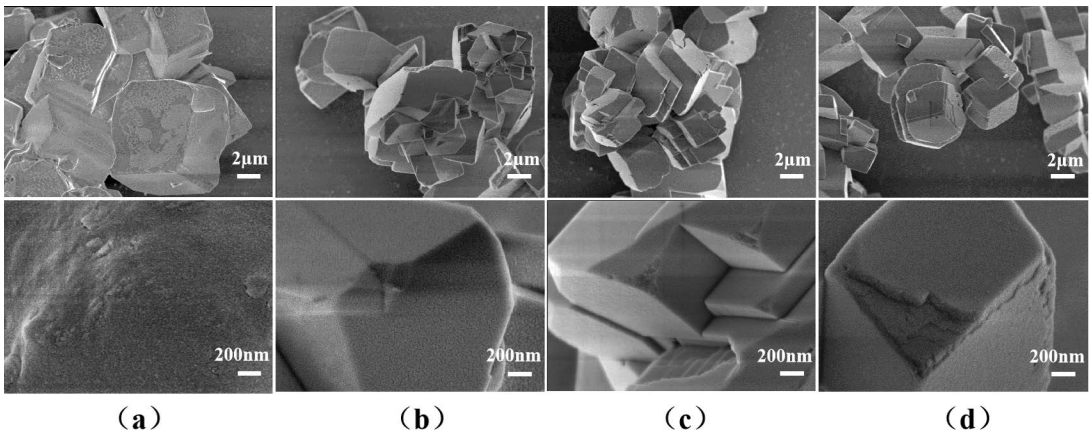

Fig. 5. Scanning electron microscopy images and the enlarged sections of calcium carbonate scale formed under different pressures: (a) 101.1 kPa, (b) 80 kPa, (c) 60 kPa and (d) 40 kPa.

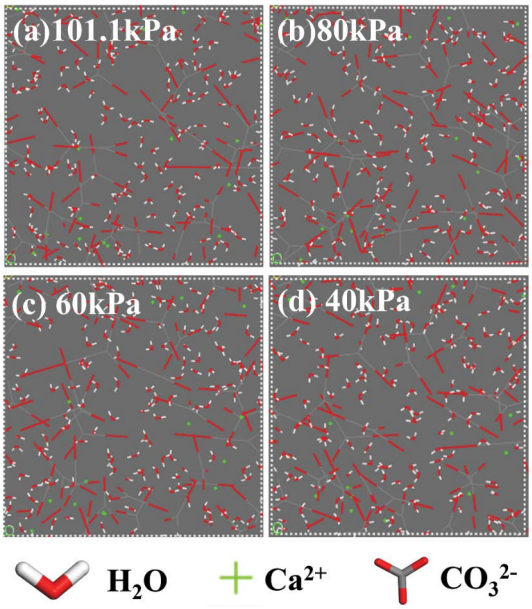

Fig. 6. Optimized results of solution under different pressures.

$$\mathrm{MSD} = \left\langle \left| r(t) - r(0) \right|^2 \right\rangle \tag{5}$$

$$D = \lim_{t \to \infty} \frac{1}{6t} \left\langle \left| r(t) - r(0) \right|^2 \right\rangle \tag{6}$$

From Fig. 7 the MSD of Ca^{2+} ions in the diffusion process under different pressures is linear with time (t). The MSD of Ca^{2+} ions increase gradually with prolong of the time. The value of diffusion coefficient (D) under negative pressure is significantly larger than that under 101.1 kPa. It indicates that the diffusion rate of Ca^{2+} ions in solution under negative pressure is obviously higher than that under 101.1 kPa. The higher diffusion rate makes it easier for $CaCO_3$ to nucleate and agglomerate. The coincidence between the test data and the fitting function is evaluated by R^2 (R related to the correlation coefficient). The values of R^2 are all greater than 0.95, which indicate that the reliability of the fitting results is relatively high. As an equilibrium system, the fluctuation range of energy should be less than 10%. As observed in Fig. 7, the four kinds of energy are all in equilibrium. Thus, the above analysis results are reliable.

According to the result of static precipitation method and EIS measurements, we have found that it is difficult to form $CaCO_3$ scale under negative pressure. And the formation amount of $CaCO_3$ is the least under 60 kPa. The formation process of $CaCO_3$ is an equilibrium process involving gas–liquid–solid phases, which is accompanied by the release of CO_2 to the atmosphere. There are the following reactions during the formation of $CaCO_3$:

$$CO_2(g) \leftrightarrow CO_2(l) \tag{7}$$

$$H_2CO_3 \leftrightarrow CO_2(l) + H_2O \tag{8}$$

$$H_2CO_3 \leftrightarrow H^+ + HCO_3^- \tag{9}$$

$$HCO_3^- \leftrightarrow H^+ + CO_3^{2-} \tag{10}$$

$$2NaHCO_3 + CaCl_2 \leftrightarrow CaCO_3 + 2NaCl + H_2CO_3 \tag{11}$$

Eqs. (7)–(11) demonstrate the ionization of carbonic acid. When the pressure decreases, the partial pressure of CO_2 in the gas phase decrease. The concentration of CO_2 in the solution is accordingly decreased and eliminates carbonic acid from the water layer. This promotes the precipitation of $CaCO_3$ scale [Eq. (11)]. The calcium carbonate solubility is therefore highly depends on the carbon dioxide content of the water [13]. On the other hand, the formation of $CaCO_3$ is accompanied by the formation of new H_2CO_3 in the solution resulting in a decrease in solution pH. The decrease of pH value is unfavorable to the formation of $CaCO_3$. Thus, under the combined effect of these two factors, the amount of $CaCO_3$ scale is least under 60 kPa, even less than that under 40 kPa.

The morphology and the size distribution of $CaCO_3$ scale have changed significantly under different pressures. A schematic diagram of this process is shown in Fig. 8.

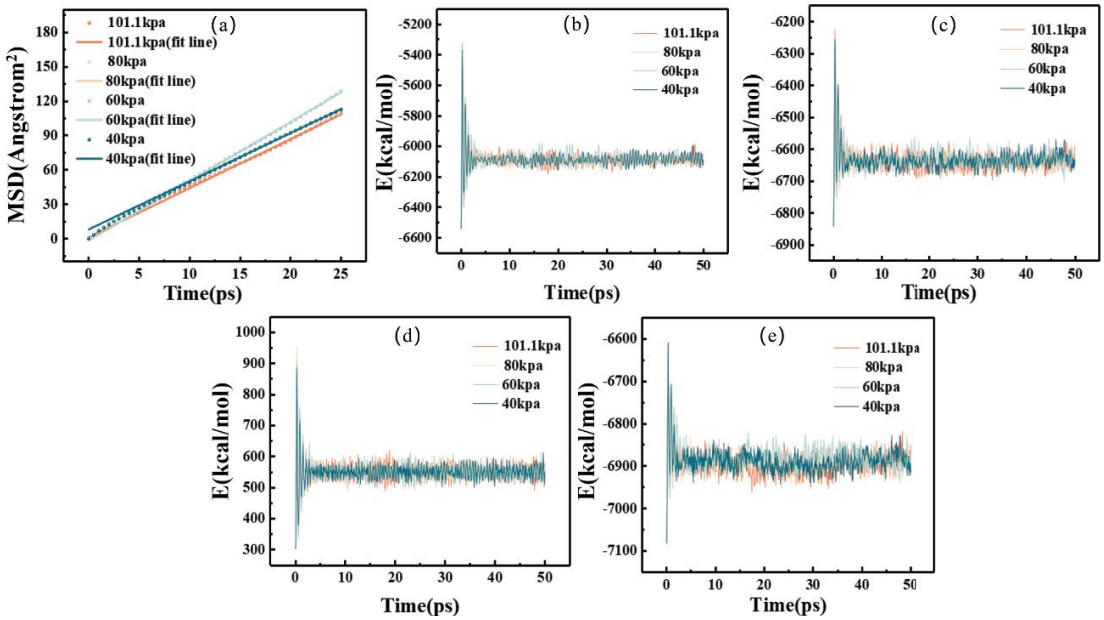

Fig. 7. Mean square displacement and fluctuations of energy during molecular simulation: (a) MSD of Ca^{2+}, (b) total energy, (c) potential energy, (d) kinetic energy and (e) non-bond energy.

Table 3
Fit data of mean square displacement of Ca^{2+} ions in solution

	101.1 kPa	80 kPa	60 kPa	40 kPa
D ($\times 10^{-8}$ m^2/s)	0.71	0.73	0.86	0.74
R^2	0.99	0.99	0.99	0.99

Under negative pressure, the distribution probability of large particles of $CaCO_3$ is greater, and the crystal surface of $CaCO_3$ is rougher. This is mainly because the pressure affects the growth process of $CaCO_3$ crystal. From Table 3, the diffusion coefficient is different under different pressure. Under 101.1 kPa, the diffusion coefficient of Ca^{2+} ions are small. And the $CaCO_3$ particles can grow into perfect

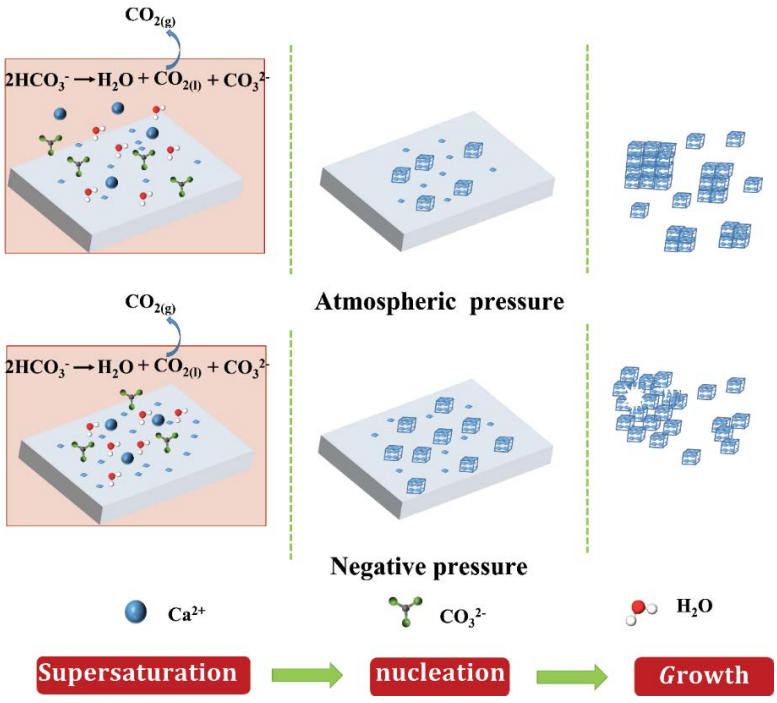

Fig. 8. Schematic diagram for effect of negative pressure on the formation of calcium carbonate.

integral particles [12]. Under negative pressure, the diffusion coefficient of Ca^{2+} ions become large. This brings a higher collision of crystal nucleus. The higher collision rate also contributes to an increase in the probability of $CaCO_3$ particles agglomeration [35]. It means that it is easier to agglomerate into large particles under negative pressure.

4. Conclusions

In summary, the formation of $CaCO_3$ scale under different operation pressure is investigated. Through the static precipitation method and the electrochemical experiment, we find that the amount of $CaCO_3$ scale formation is less under negative pressure, especially under 60 kPa. However, the distribution probability of large particles of $CaCO_3$ under 60 kPa is the largest. The Ca^{2+} ions have the diffusion coefficient under different operation pressure. Under negative pressure, the higher diffusion coefficient of Ca^{2+} ions bring a higher collision of crystal nucleus. The higher collision rate also contributes to an increase in the probability of $CaCO_3$ particles agglomeration. Aggregation of particles results in the increase of the $CaCO_3$ particle size. This study provided some guidance value for exploring the scale inhibition technology under negative pressure operation, such as the low temperature multi-effect distillation (LT-MED) desalination process.

Acknowledgments

Our work was supported by NSFC project (Grant No 52071198). We thank the grant from the Science & Technology Commission of Shanghai Municipality (18DZ2204400, 19DZ2271100) very much.

References

[1] M.W. Shahzad, M. Burhan, A. Li, K.C. Ng, Energy-water-environment nexus underpinning future desalination sustainability, Desalination, 413 (2017) 52–64.
[2] H. Wang, X.Y. Jiang, Legal measures to reduce marine environmental risks of seawater desalination in China, Nat. Resour. Forum, 44 (2020) 129–143.
[3] A. Ophir, F. Lokiec, Advanced MED process for most economical sea water desalination, Desalination, 182 (2005) 187–198.
[4] M.W. Shahzad, K. Thu, Y.-d. Kim, K.C. Ng, An experimental investigation on MEDAD hybrid desalination cycle, Appl. Energy, 148 (2015) 273–281.
[5] D.Z. Yang, J.H. Liu, X.E. Xiao, L.L. Jiang, Experimental study of composition and influence factors on fouling of stainless steel and copper in seawater, Ann. Nucl. Energy, 94 (2016) 767–772.
[6] A. Al-Karaghouli, L.L. Kazmerski, Energy consumption and water production cost of conventional and renewable-energy-powered desalination processes, Renewable Sustainable Energy Rev., 24 (2013) 343–356.
[7] M. Alhaj, M. Abdelnasser, S.G. Al-Ghamdi, Energy efficient multi-effect distillation powered by a solar linear Fresnel collector, Energy Convers. Manage., 171 (2018) 576–586.
[8] S. Liu, Z. Wang, M. Han, J.J. Zhang, Embodied water consumption between typical desalination projects: reverse osmosis versus low-temperature multi-effect distillation, J. Cleaner Prod., 295 (2021) 126340, doi: 10.1016/j.jclepro.2021.126340.
[9] S.M. Parsa, M. Majidniya, W.H. Alawee, H.A. Dhahad, H.M. Ali, M. Afrand, M. Amidpour, Thermodynamic, economic, and sensitivity analysis of salt gradient solar pond (SGSP) integrated with a low-temperature multi effect desalination (MED): case study, Iran, Sustainable Energy Technol. Assess., 47 (2021) 101478, doi: 10.1016/j.seta.2021.101478.
[10] M.S. Kamal, I. Hussein, M. Mahmoud, A.S. Sultan, M.A.S. Saad, Oilfield scale formation and chemical removal: a review, J. Pet. Sci. Eng., 171 (2018) 127–139.
[11] D.Z. Yang, J.H. Liu, X.E. Xiao, L.L. Jiang, Model for seawater fouling and effects of temperature, flow velocity and surface free energy on seawater fouling, Chin. J. Chem. Eng., 24 (2016) 658–664.
[12] S.J. Dyer, G.M. Graham, The effect of temperature and pressure on oilfield scale formation, J. Pet. Sci. Eng., 35 (2002) 95–107.
[13] M.-A. Ahmadi, A. Bahadori, S.R. Shadizadeh, A rigorous model to predict the amount of dissolved calcium carbonate concentration throughout oil field brines: side effect of pressure and temperature, Fuel, 139 (2015) 154–159.
[14] H.C. Jin, X.J. Zhang, Y. Yu, X.M. Chen, High-performance Ti/IrO_2-RhO_3-TiO_2/α-PbO_2/β-PbO_2 electrodes for scale inhibitors degradation, Chem. Eng. J., 435 (2022) 135167, doi: 10.1016/j.cej.2022.135167.
[15] T.R. Mattsson, J.M.D. Lane, K.R. Cochrane, M.P. Desjarlais, A.P. Thompson, F. Pierce, G.S. Grest, First-principles and classical molecular dynamics simulation of shocked polymers, Phys. Rev. B: Condens. Matter, 81 (2010) 054103, doi: 10.1103/physrevb.81.054103.
[16] Y.W. Zuo, W.Z. Yang, K.G. Zhang, Y. Chen, X.S. Yin, Y. Liu, Experimental and theoretical studies of carboxylic polymers with low molecular weight as inhibitors for calcium carbonate scale, Crystals, 10 (2020) 406, doi: 10.3390/cryst10050406.
[17] G.C. Sosso, J. Chen, S.J. Cox, M. Fitzner, P. Pedevilla, A. Zen, A. Michaelides, Crystal nucleation in liquids: open questions and future challenges in molecular dynamics simulations, Chem. Rev., 116 (2016) 7078–7116.
[18] Y. Guo, Z.H. Chen, X.S. Yin, W.Z. Yang, Y. Chen, Y. Liu, Effect of the passive films on $CaCO_3$ scale depositing on Q235 steel: electrochemical and surface investigation, J. Colloid Interface Sci., 611 (2022) 172–182.
[19] Z.S. Zuo, W.Z. Yang, K.G. Zhang, Y. Chen, M. Li, Y.W. Zuo, X.S. Yin, Y. Liu, Effect of scale inhibitors on the structure and morphology of $CaCO_3$ crystal electrochemically deposited on TA1 alloy, J. Colloid Interface Sci., 562 (2020) 558–566.
[20] C. Barchiche, C. Deslouis, D. Festy, O. Gil, Ph. Refait, S. Touzain, B. Tribollet, Characterization of calcareous deposits in artificial seawater by impedance techniques: 3—Deposit of $CaCO_3$ in the presence of Mg(II), Electrochim. Acta, 48 (2003) 1645–1654.
[21] X.M. Xu, Y.B. Chen, W. Zhou, Z.H. Zhu, C. Su, M.L. Liu, Z.P. Shao, A perovskite electrocatalyst for efficient hydrogen evolution reaction, Adv. Mater., 28 (2016) 6442–6448.
[22] M. Piri, R. Arefinia, Investigation of the hydrogen evolution phenomenon on $CaCO_3$ precipitation in artificial seawater, Desalination, 444 (2018) 142–150.
[23] R. Ketrane, L. Leleyter, F. Baraud, M. Jeannin, O. Gil, B. Saidani, Characterization of natural scale deposits formed in southern Algeria groundwater. Effect of its major ions on calcium carbonate precipitation, Desalination, 262 (2010) 21–30.
[24] J. Marín-Cruz, R. Cabrera-Sierra, M.A. Pech-Canul, I. González, EIS characterization of the evolution of calcium carbonate scaling in cooling systems in presence of inhibitors, J. Solid State Electrochem., 11 (2007) 1245–1252.
[25] O. Devos, C. Gabrielli, B. Tribollet, Simultaneous EIS and *in-situ* microscope observation on a partially blocked electrode application to scale electrodeposition, Electrochim. Acta, 51 (2006) 1413–1422.
[26] R. De Motte, E. Basilico, R. Mingant, J. Kittel, F. Ropital, P. Combrade, S. Necib, V. Deydier, D. Crusset, S. Marcelin, A study by electrochemical impedance spectroscopy and surface analysis of corrosion product layers formed during CO_2 corrosion of low alloy steel, Corros. Sci., 172 (2020) 108666, doi: 10.1016/j.corsci.2020.108666.
[27] Z.C. Chen, S. Xiao, F. Chen, D.Z. Chen, J.L. Fang, M. Zhao, Calcium carbonate phase transformations during the carbonation reaction of calcium heavy alkylbenzene sulfonate over-based nanodetergents preparation, J. Colloid Interface Sci., 359 (2011) 56–67.
[28] F. Bosch Reig, J.V. Gimeno Adelantado, M.C.M. Moya Moreno, FTIR quantitative analysis of calcium carbonate (calcite)

and silica (quartz) mixtures using the constant ratio method. Application to geological samples, Talanta, 58 (2002) 811–821.
[29] X. Chen, V. Achal, Effect of simulated acid rain on the stability of calcium carbonate immobilized by microbial carbonate precipitation, J. Environ. Manage., 264 (2020) 110419, doi: 10.1016/j.jenvman.2020.110419.
[30] C.G. Kontoyannis, N.V. Vagenas, Calcium carbonate phase analysis using XRD and FT-Raman spectroscopy, Analyst, 125 (2000) 251–255.
[31] Z.Y. Zou, W.J.E.M. Habraken, G. Matveeva, A.C.S. Jensen, L. Bertinetti, M.A. Hood, C.-Y. Sun, P.U.P.A. Gilbert, I. Polishchuk, B. Pokroy, J. Mahamid, Y. Politi, S. Weiner, P. Werner, S. Bette, R. Dinnebier, U. Kolb, E. Zolotoyabko, P. Fratzl, A hydrated crystalline calcium carbonate phase: calcium carbonate hemihydrate, Science, 363 (2019) 396–400.
[32] Y.Y. Wang, Y.J. He, J. Zhan, Z.P. Li, Identification of soil particle size distribution in different sedimentary environments at river basin scale by fractal dimension, Sci. Rep., 12 (2022) 10960, doi: 10.1038/s41598-022-15141-6.
[33] X.W. Song, L. Zhang, Y.W. Cao, J.H. Zhu, X.P. Luo, Effect of pH and temperatures on the fast precipitation vaterite particle size and polymorph stability without additives by steamed ammonia liquid waste, Powder Technol., 374 (2020) 263–273.
[34] C. Shen, X. Xu, X.-Y. Hou, D.-X. Wu, J.-H. Yin, Molecular weight effect on PAA antiscale performance in LT-MED desalination system: static experiment and MD simulation, Desalination, 445 (2018) 1–5.
[36] R. Beck, J.-P. Andreassen, The onset of spherulitic growth in crystallization of calcium carbonate, J. Cryst. Growth, 312 (2010) 2226–2238.

Supplementary information

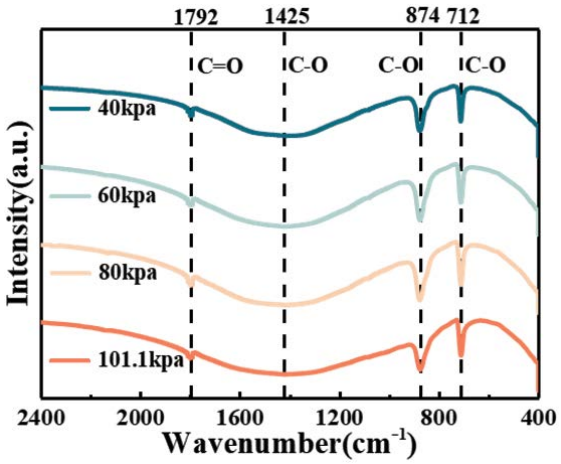

Fig. S1. FTIR spectra of calcium carbonate scales obtained under different pressures.

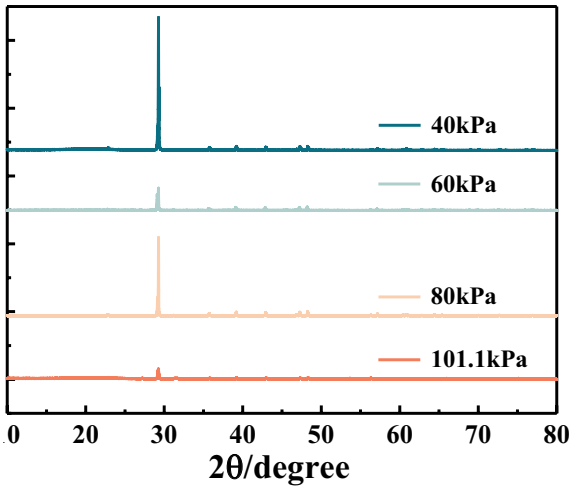

Fig. S2. X-ray diffraction patterns of the calcium carbonate scale obtained under different pressures.

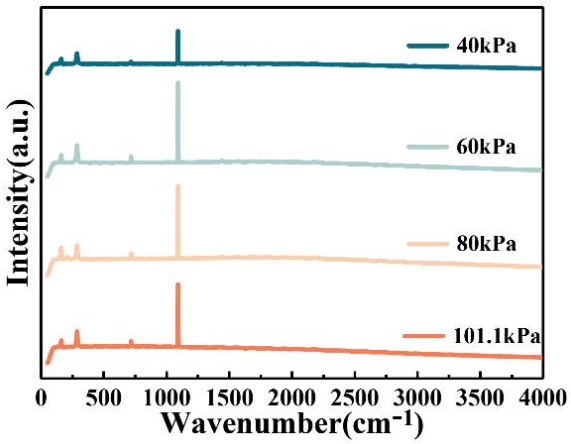

Fig. S3. Raman spectra of calcium carbonate scales obtained under different pressures.